

Optical illumination optimization for patterned defect inspection

Bryan M. Barnes*, Richard Quintanilha, Yeung-Joon Sohn, Hui Zhou, and Richard M. Silver
Physical Measurement Laboratory, National Institute of Standards and Technology,
100 Bureau Dr. MS 8212, Gaithersburg, MD USA 20899-8212

ABSTRACT

Rapidly decreasing critical dimensions (CD) for semiconductor devices drive the study of improved methods for the detection of defects within patterned areas. As reduced CDs are being achieved through directional patterning, additional constraints and opportunities present themselves in defect metrology. This simulation and experimental study assesses potential improvements in patterned defect inspection that may be achieved by engineering the light incident to the sample within a high-magnification imaging platform. Simulation variables include the incident angle, polarization, and wavelength for defect types common to directional device layouts. Detectability is determined through differential images between no-defect- and defect-containing images. Alternative metrologies such as interference microscopy are also investigated through modeling. The measurement of a sub-20 nm defects is demonstrated experimentally using 193 nm light. The complex interplay of unidirectional patterning and highly directional defects is explored using structured off-axis illumination and polarization.

Keywords: Defect detection, Scatterfield optical microscopy, illumination optimization, bright-field microscopy, dark-field microscopy

1. INTRODUCTION

Challenges facing the practical, continued progression of Moore's Law are in part due to defect metrology requirements of high-volume manufacturing at ever-decreasing critical dimensions (CD). An ever-present requirement for defect metrology is to be able to identify the presence of a defect with dimensions on the scale of or less than the CD. Another ongoing goal has been the identification of defects within patterned devices that feature dense, highly complex shapes in two dimensions on the wafer with periodicity greater than the wavelength of the inspection tool. The extension of 193 nm immersion lithography techniques using highly directional reticles and dipole illumination has altered the design characteristics of devices. These designs have produced another challenge for defect metrology, the identification of defects within patterned devices that feature dense arrays of line segments oriented along a single, preferred direction where the line segment pitch is near to the optical wavelength.

Our group has previously reported [1] simulations on the detectability of certain defect types as a function of incident angle for the 65nm and 32 nm node SEMATECH Intentional Defect Arrays (IDA). The defect-free patterns of the 32 nm node IDA is much more unidirectional than the previous 65 nm version. Within these 32 nm IDA targets, defects were identified as having either a low directionality or a high directionality. Low directionality defects such as islands showed little increase in detectability as the azimuthal angle was changed from $\phi = 0^\circ$ (light parallel to the preferred direction) to $\phi = 90^\circ$ (light perpendicular to the preferred direction.) However, a highly directional bridge defect spanning two lines was much more detectable using light parallel to the primary features but perpendicular to the bridge.

The goal of this present work is to investigate the roles of wavelength, angle, and polarization for two key defect types found on unidirectional layouts, line-to-line and end-to-end defects, using electromagnetic scattering calculations and experimental measurements. In Section 2, key details of our particular optical microscopy technique, called scatterfield microscopy, are reviewed to establish the modeling constraints and experimental capabilities. The various three-dimensional electromagnetic simulation models are reviewed in Section 3. These simulation results are shown in Section 4, with simulated defects observed by subtracting images calculated with and without a defect present. Section 5 outlines a possible alternative microscopy method for defect detection, interference microscopy. The experimental section, Section 6, features images from intentional defect arrays collected on the NIST 193 nm microscope.

*bryan.barnes@nist.gov; phone 1 301 975-3947; fax 1 301 869 0822; www.nist.gov/pml/div681/om.cfm

2. SCATTERFIELD OPTICAL MICROSCOPY

Scatterfield optical microscopy (SOM) is essentially the implementation of scatterometry on a high-magnification platform. Full details on the Scatterfield technique and associated approaches for performing illumination optimization have been published elsewhere.[2][3] As a brief introduction, SOM permits angle-resolved scanning within a microscope by utilizing the properties of Köhler illumination, outlined schematically in Fig. 1. One can control the angle of incidence at the object focal plane by manipulating the light entering the back focal plane of the condenser lens. In a microscope, this object focal plane is the sample plane while the condenser is its objective lens. Control of the angle of incidence at the sample is achieved in our microscopes by relaying out and magnifying this plane to yield a conjugate to the back focal plane (CBFP) where aperture(s) can be used to permit a limited range of angles to proceed through the illumination path. In the schematic below, three points in the source plane (A, B, and C) are focused onto the back focal plane. If at the back focal plane, or its conjugate, light from points A and B is blocked while light from point C is allowed to pass, then the resulting illumination is off-axis at a definable angle. Mapping of CBFP aperture position to the resultant angle of incidence is performed as a calibration step for angle-resolved imaging.

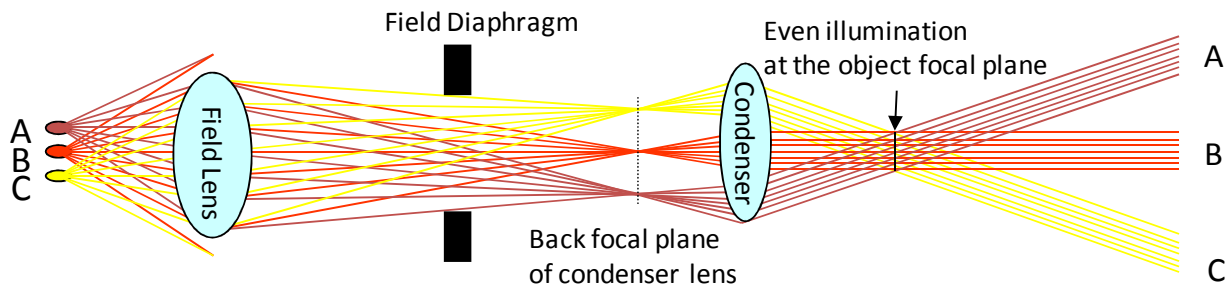


Figure 1. Schematic for a Köhler illumination. While the general use of Köhler illumination is to illuminate a sample homogeneously even if the source is inhomogeneous, Köhler also permits illumination engineering, such as off-axis illumination, within scatterfield microscopes.

Furthermore, the light from each point source is a plane wave at the sample. In the simulations that follow, a single plane wave with a linear polarization illuminates the sample at a single angle of incidence and is reflected off these modeled targets. Quantitative comparison with experimental results requires a full accounting of the finite aperture(s) used for illumination through the simulation of several well-chosen plane waves about a mean angle. Due to the computationally intensive nature of these simulations, as described below, such comparison lies beyond the scope of this paper. The simulation results will however illustrate trends to be observed in the experimental results that follow.

3. 3-D SIMULATIONS USING OPTIMIZED ILLUMINATION

The modeling of scattering from defect targets requires the use of three-dimensional electromagnetic simulators. Two general methods are used in the present work: the finite-difference time-domain (FDTD) method [4] and a finite element method (FEM) [5] Maxwell's equations solver. Commercial software packages were used for both models, while an in-house FDTD code has been developed to provide a benchmark for the commercial packages and to provide greater insight into the modeling physics of these three dimensional codes.

Whether using FEM or FDTD, the result of a simulation is an aerial image of the defect target. As the illumination wavelength is much larger than the critical dimensions, individual features are said to be unresolved as seen in Fig. 2a and 2b, though it can be seen that a pattern in this example is repeated 3x vertically and 4x horizontally within the image. The difference between Figs. 2a and 2b is that one defect has been placed in one of the twelve repeats of this pattern in Fig. 2b. Fig. 2c is the absolute value of the differential image of the previous two images, plotted with a different intensity scale for clarity. The scattering effects of this defect extend beyond the pattern in which it was placed, which necessitated the addition of a buffer layer of non-defect containing cells around it. Care must be taken when defining the size of the simulation domain, as both FDTD and FEM assume periodic boundary conditions. With these conditions, as the simulation domain size is decreased, there is a greater likelihood for resonance of the optical signal of the defect due to its periodicity, thus artificially amplifying the defect detectability.

These differential images are manipulated to yield the defect detectability. To facilitate the analysis of several defects, angles, polarizations, *etc.* at once, it is useful to introduce a figure-of-merit (FOM). For example, the resultant differential image in Fig. 2c. can be reduced to a FOM by performing the mean of all pixels in the image.

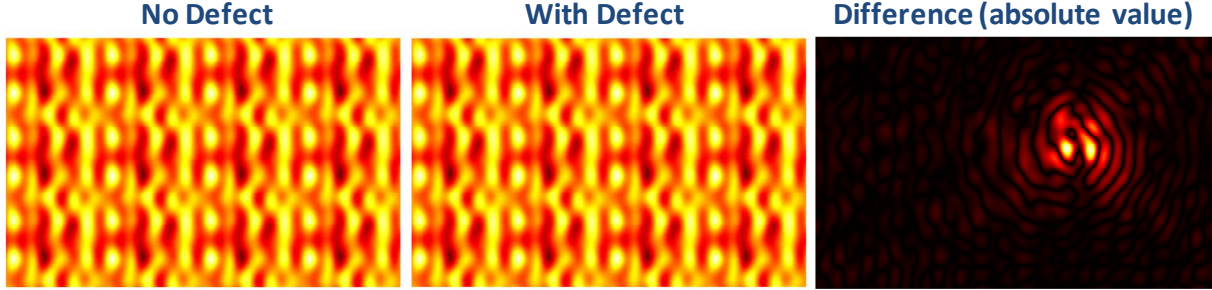


Figure 2. Results subtracted for die-to-defect comparisons. Interference among the periodic defects is reduced by introducing a “buffer layer” of no-defect unit cells as these simulations assume periodic boundary conditions. This example was simulated using a 32 nm SEMATECH intentional defect array structure for $\lambda = 193$ nm light.

Targets similar to those used in this defect study are shown schematically in Fig. 3a. The uniaxial directionality of these patterned arrays leads to two specific types of extrusion defects: line-to-line and end-to-end. These defects are themselves highly directional and will be simulated using a variety of incident angles. Specifically, with engineered illumination the incident angles are combinations of polar and azimuthal angles as illustrated in Fig. 3b.

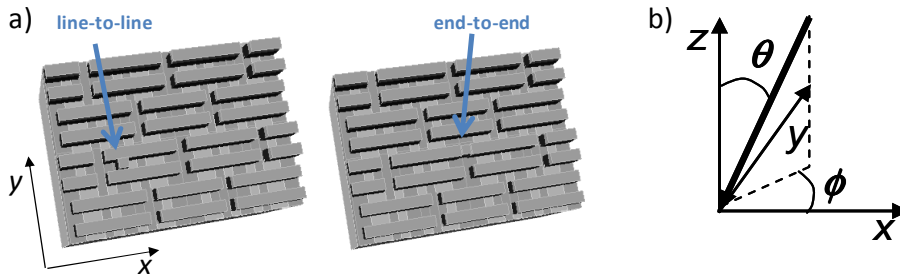


Figure 3. a) Schematic of defect types simulated. As these underlying structures have a strong x-y directionality, azimuthal angles between $\phi = 0^\circ$ (along the lines) and $\phi = 90^\circ$ (across the lines) are simulated. These two defects are highly directional. Simulations were performed for a variety of CD values. Panel a) includes graphics from Ref. [6].

4. COMPARISONS USING DIE-TO-DEFECT METROLOGY

In this section, the effects of incident angle, polarization, and wavelength for these two defect types are explored. While the interactions among defect type, incident angle, and polarization are complex, the effect of wavelength is more straightforward. FDTD simulations of both the line-to-line and end-to-end structures above were performed for $\lambda = 193$ nm and $\lambda = 450$ nm using both TE and TM polarizations. Structure CD was varied from 22 nm to 40 nm. While defect detectability varied with polarization and angle at $\lambda = 193$ nm, the differential images calculated for $\lambda = 450$ nm showed almost no variation or modulation due to the presence of a defect. Therefore, all simulations below were performed for $\lambda = 193$ nm.

Simulations were performed at 43 points in the conjugate back focal plane for a comprehensive overview. From these CBF locations, the resultant incident polar angles ranged from $\theta = 0^\circ$ to $\theta = 80^\circ$ while the incident azimuthal angle ranged from $\phi = 0^\circ$ to $\phi = 90^\circ$. These simulations were performed for both end-to-end and line-to-line defects, and the mean intensities of the image were taken as the FOM. Results are shown in Figs. 4 and 5 on the following page.

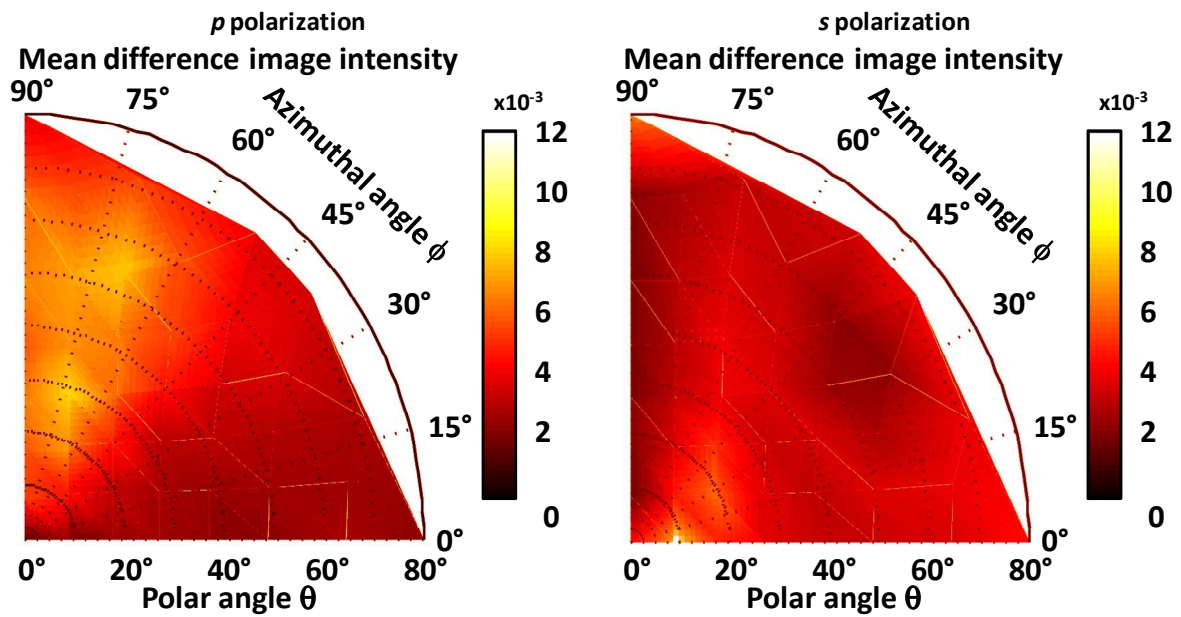


Figure 4. Defect detectability for an end-to-end defect as a function of polarization and incident angle. The mean intensity of difference images is used as the figure-of-merit (FOM). High azimuthal angles with p polarization are best for detection here. Results are from FEM simulations on a 40 nm CD structure illuminated at $\lambda = 193$ nm.

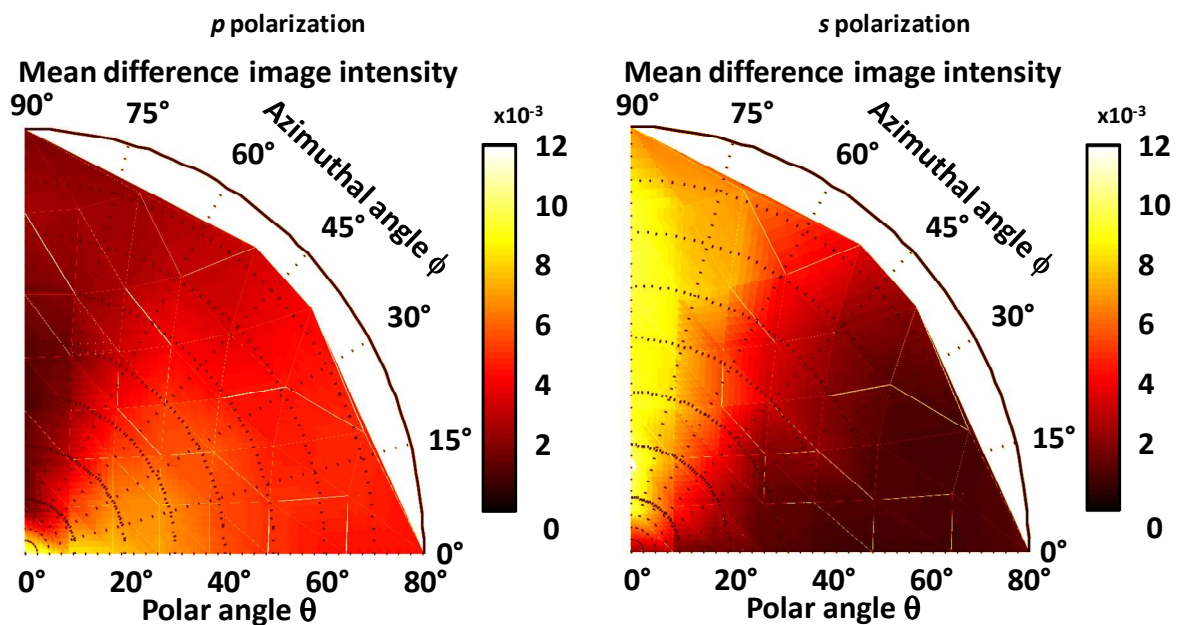


Figure 5. Defect detectability for a line-to-line defect as a function of polarization and incident angle. The mean intensity of difference images is used as the figure-of-merit (FOM). High azimuthal angles with s polarization are best for detection here. This best polarization is orthogonal to that above, just as the defects are orthogonal in direction to each other. Results are from FEM simulations on a 40 nm CD structure illuminated at $\lambda = 193$ nm.

Figure 4 shows two polar plots of the detectivity figure-of-merit for the end-to-end defect as simulated using FEM on a 40 nm CD structure. On the left is the plot for illumination using p-polarization, at right, s-polarization. For the p-polarization, the lighter regions (indicating a larger FOM) correlate to simulations using high azimuthal ($\phi > 75^\circ$) angles. The FOM values appear to be less on average in the s polarization graph. For the line-to-line defect results in Fig. 5, the polarization results are reversed – there is strong defect detectability for s-polarized light using high azimuthal while p-polarization is less effective (lesser FOM) and somewhat preferential to low azimuthal angles.

These polarization results can be compared favorably to trends reported by Meshulach, *et al.* [7] for simulations of similar defect types using $\lambda \geq 266$ nm with normal incidence illumination and fixed collection numerical apertures (*i.e.* fixed angles). They derived from first principles that sub-wavelength structures exhibit form birefringence, impacting the scattering which can be enhanced with polarization control. Specifically, they simulated that line-to-line defects were enhanced using polarization perpendicular to the dominant line direction while line cut defects (the incursion equivalent of an end-to-end excursion) showed highest scattering for polarization that was parallel to the dominant line direction. [9] Our results indicate that the preferred combination of angle and polarization for an end-to-end defect is high-azimuthal angle p polarization, which is perpendicular to the primary direction of both the line and the defect. Likewise, s-polarization at high azimuthal angles for the line-to-line defect translates to a polarization parallel to the lines and perpendicular to the defect.

5. INTERFERENCE MICROSCOPY FOR DEFECT METROLOGY

In addition to varying polarization and angle for different defect types we investigated another option using modeling for improved defect detectability. Figure 6 below shows a schematic of one possible interference microscope configuration for defect detection. The design features a reference plane which reflects the light passing through a beamsplitter. Meanwhile, light on the illumination path enters the objective and is reflected from the sample. At the beamsplitter the two reflected beams are directed toward a charge-coupled device (CCD) camera, where the two beams are interfered and the subsequent intensity measured. This interference can be repeated for known non-defect target and a defect target, allowing again for the computation of a differential image.

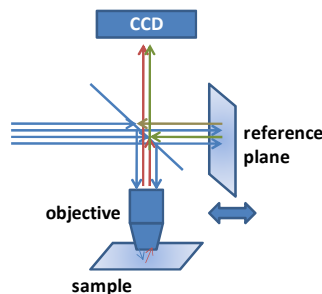


Figure 6. Schematic of an interference microscope used for this simulation study. If a second objective were placed before the reference plane, the result would be the well-known Linnik-type interference microscope. Reflection from a second objective was not used here to assess whether detectability could be improved without the added cost and complication of a second objective designed for $\lambda = 193$ nm.

Movements of the reference plane produce a phase shift angle from 0° to 360° . The contrast between the defect and the underlying structure changes with phase angle. Interference microscopy simulations were conducted using the FEM model for 22 nm, 30 nm, and 40 nm CD structures and both end-to-end and line-to-line defects. One example for a 22nm end-to-end defect is shown in Fig. 7. The FOM has been adjusted by dividing by the total number of pixels. The dashed line, constant as a function of phase angle, represents the FOM of the difference image without the use of interference microscopy. The large dots represent the difference image FOM values for various phase angles. A spline fit, the dotted line, connects these points.

In this example, there are regions of the phase angle for which the use of interference microscopy hinders defect detectability. At 120° phase angle, the FOM is at its lowest and the defect disappears from the difference image shown in Fig. 7. At 300° phase angle, the defect is most apparent. The FOM increases by a factor of 2x, and the defect signal in the difference image of the defect is more easily determined.

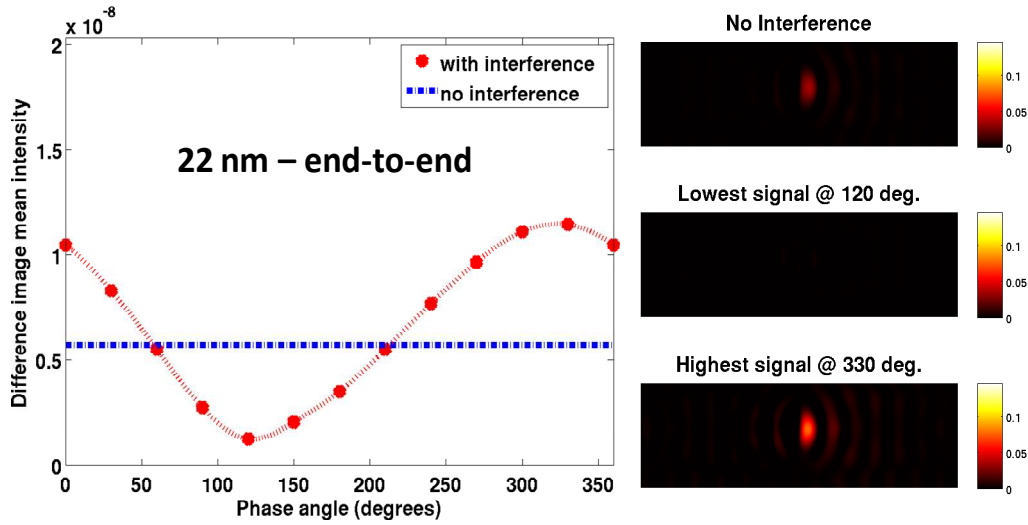


Figure 7. Defect detectability figure-of-merit as a function of phase angle, with difference images. (left) The FOM calculated without interference microscopy is the dashed, flat line. The FOM from interference microscopy difference images is shown as the large dots. (right) Difference images illustrate the worst and best cases using interference compared to using standard microscopy methods. Simulations were performed using FEM.

6. DEFECT DETECTION EXPERIMENTS

Two intentional defect array (IDA) wafers were measured. In Fig. 8 below, the SEMATECH 65 nm Metal-1 IDA is used to show the effects of limiting the incident polar angle upon defect detectability.

The NIST 193 nm Microscope [8] is a reflection microscope with an ArF excimer laser as its source. Coherence is broken using a rotating diffuser at the source plane of the Köhler layout. The microscope features a 12 mm diameter CBFP and a catadioptric objective lens which limits the numerical aperture range from an inner value of $NA = 0.11$ to an outer value of $NA = 0.74$. This range corresponds to a possible polar angular range of $\theta = 6^\circ$ to 47° .

The illumination numerical aperture (INA) and thus the polar angle range were adjusted by centering apertures of various sizes in the CBFP. In Fig. 8, experimental difference images are shown for annular illuminations ranging from a maximum θ_{outer} angle of 47° to a minimum of 22° , ($INA_{outer} = 0.74$ to 0.37) while not affecting the inner INA. Limiting the polar angular range appears to sharpen and increase the signal from a known defect inside the circle of each image. The defect size was determined using scanning electron microscopy (SEM) to have a critical dimension of 17 nm.

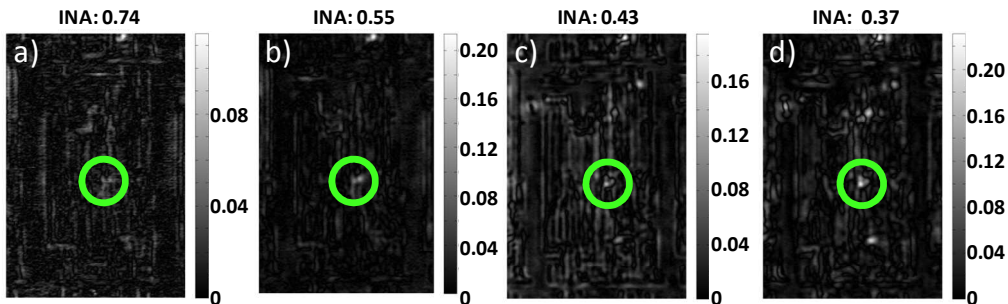


Figure 8. Normalized, absolute value differential images of a 17 nm-sized defect on the SEMATECH 65 nm Metal-1 Intentional Defect Array wafer. Sample was illuminated with unpolarized $\lambda = 193$ nm light, with the illumination numerical aperture (INA) varied among these measurements. Illumination polar angle ranges are a) 6° to 47° , b) 6° to 33° , c) 6° to 25° , and d) 6° to 22° . Defect is shown within the circle and is more detectable as the angular range is decreased. Defect size was determined by SEM measurement.

Given a sufficient collection numerical aperture (CNA), high INA annular illumination leads to enhancements in resolution and visibility as higher order diffracted light is produced upon reflection. However, it is when lower INA values are used that this defect appears sharper. It is possible that the catadioptric objective blocks the higher order diffracted beam either near normal incidence (CNA = 0 to 0.11 is blocked) or at higher angles (CNA = 0.74 and above is inaccessible.) It is more likely that the broader cone shape yields a lower contrast as multiple lower spatial frequency beams contribute to the background distribution in the image, producing a blurring effect. As the incident cone of light is reduced in INA, the higher order diffracted beams needed for defect detection are captured by the objective lens.

A second IDA wafer was measured featuring nominal CD values of 30 nm. Illumination was engineered using a dipole or a polarizer. Figure 9 shows the unresolved images of structures similar to those shown in Fig. 3a. The number beside each defect target indicates the nominal size of the defect contained within. The defect is centered within each target.

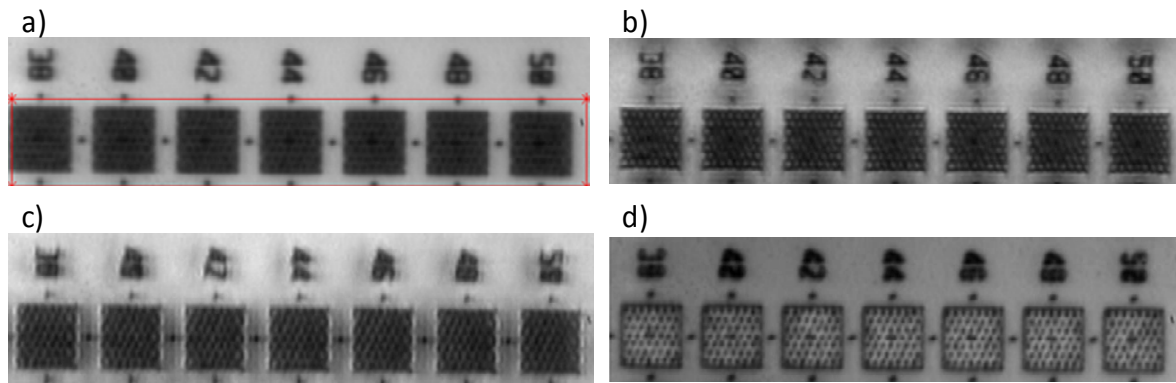


Figure 9. Images of targets in an intentional defect array as measured at $\lambda = 193$ nm. The sample is illuminated with unpolarized light in Panels a), b), and c) with various structured illumination: a) Full-field illumination, b) Dipole illumination parallel to the lines, c) Dipole illumination perpendicular to lines. Panel d) was illuminated using full-field illumination and linearly polarized ($\phi = 45^\circ$ with respect to lines) light.

Fig. 9a shows nominal line-to-line defects 38 nm to 50 nm as illuminated by unpolarized, full field illumination. This measurement serves as a benchmark against which to compare the effects on detectability of engineering the illumination. A black dot at the center of the target, from the defect, is obscured by the target's interior structure. As the data in Figs. 5 and 6 indicated strong sensitivity to azimuthal angle, a dipole with INA = 0.58 to 0.74 ($\theta = 36^\circ$ to 47°) and azimuthal angular width $\Delta\phi = \pm 45^\circ$ was placed in the CBFP. For Fig. 9b, the orientation of the dipole was such that the light illuminated the targets parallel to the lines ($\phi = -45^\circ$ to 45°) while for Fig. 9c, the orientation of the dipole was rotated and centered about $\phi = 90^\circ$ ($\phi = 45^\circ$ to 135°) illuminating perpendicular to the lines. The dipole was then removed and a polarizer / analyzer combination was inserted in the illumination and collection paths, respectively. For the illumination path, the linear polarizer was set at an angle of $\phi = 45^\circ$ relative to the azimuthal with the collection polarizer similarly positioned in angle.

The defect is visible in both Figs. 9b) and 10b), the image and normalized difference image, respectively, from using dipole illumination along the direction of the line segment array. However the defect is not detected using light that is perpendicular to the lines as shown in Figs. 9c) and 10c). Experimentally, with unpolarized light these line-to-line defects are best detected using an illumination angle across the defect and along the lines.

The sensitivity of the reflected image to polarization, specifically linear polarization at $\phi = 45^\circ$, does not follow from the simulations presented. Inspecting Fig. 6, data are presented for s polarization and p polarization. For s polarization, the preferred azimuthal angle is $\phi = 0^\circ$ and for p polarization, $\phi = 90^\circ$. Both indicate that the best linear polarization should be perpendicular to the defect and parallel to the lines. This discrepancy is the subject of continued study.

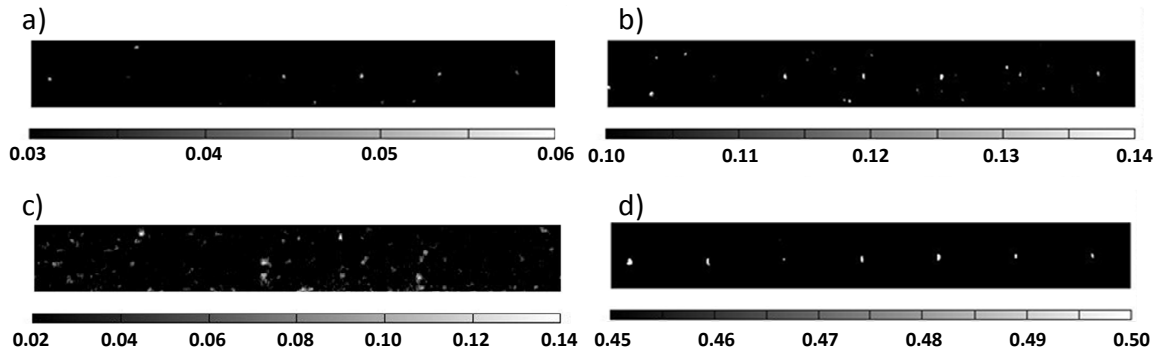


Figure 10. Normalized difference images between defects in Fig. 9 and non-defects targets. Thresholding has been applied to accentuate the defects. The best detectability is found in d) full-field $\varphi = 45^\circ$ linear polarization, followed by b) unpolarized dipole parallel to lines, and a) unpolarized full-field. The defects are not visible in c) unpolarized dipole perpendicular to the lines.

7. SUMMARY

Scatterfield microscopy enables signal-based and die-to-die defect analysis of features with sub-wavelength dimensions by engineering the illumination and analysis of the entire scattered field. Simulations were performed using three-dimensional electromagnetic simulation packages considering several parameters, such as the illumination wavelength, polarization, and angle of incidence. Angle and polarization resolved enhancements of the defect sensitivity were demonstrated in simulation. Consideration of the polarization, defect type, and incident angle are crucial when seeking the optimum illumination for a specific defect, as no one set of parameters will optimize all defects equally. Interference microscopy was shown to enhance detectability in the modeling. Experimental measurement of a sub-20 nm defect was enhanced through polar angular manipulation. Detectability improvement via a change in azimuthal angle was shown.

ACKNOWLEDGEMENTS

The authors wish to thank the SEMATECH Metrology Initiative for access to intentional defect array wafers and for funding support.

REFERENCES

- [1] Silver, R.M., Barnes, B. M., Sohn, Y.-J., Quintanilha, R., Zhou, H., Deeb, C., Johnson, M., Goodwin, M. and Patel, D., "The limits and extensibility of optical patterned defect inspection", Proc. SPIE 7638, 76380J (2010).
- [2] Barnes, B. M., Howard, L., and Silver, R. M., "Illumination optimization for optical semiconductor metrology", Proc. SPIE 6289, 62890P (2006).
- [3] Barnes, B. M., Attota, R., Quintanilha, R., Sohn Y.-J., and Silver, R. M., "Characterizing a scatterfield optical platform for semiconductor metrology," Meas. Sci. Technol. 22, 024003 (2011).
- [4] Taflove A., "Application of the Finite-Difference Time-Domain Method to Sinusoidal Steady-State Electromagnetic-Penetration Problems," Electromagnetic Compatibility, IEEE Transactions on EMC-22, 191-202 (1980).
- [5] Schmidt, F., "An adaptive approach to the numerical solution of Fresnel's wave equation," IEEE J. Lightwave Technol. 11, 1425-1434 (1993).
- [6] Crimmins, T.F., "Defect metrology challenges at the 11-nm node and beyond", Proc. SPIE 7638, 76380H (2010).
- [7] Meshulach, D., Dolev, I., Yamazaki, Y., Tsuchiya, K., Kaneko, M., Yoshino, K., and Fujii, T., "Advanced lithography – Wafer defect scattering analysis at DUV," Proc. SPIE 7638, 76380K (2010).
- [8] Sohn, Y.-J. Quintanilha, R., Barnes, B. M., and Silver, R.M. "193 nm angle-resolved scatterfield microscope for semiconductor metrology," Proc. SPIE 7405, 74050R (2009).